Electronic Supplementary Material (ESI) for Journal of Materials Chemistry A.
This journal is © The Royal Society of Chemistry 2022

Supporting Information

Macromonomer Crosslinking Polymerized Scaffolds for Mechanically Robust and Flexible Perovskite Solar Cells

Tangyue Xue,[‡a,b] Duo Chen,[‡c] Meng Su,*[b] Xiaotian Hu,*[d] Zengqi Huang,[b] Tingqing Wu,[b] Guanghui Yu,[e] Ke-Jian Jiang,[b] Yiqiang Zhang,*[e] and Yanlin Song*[b]

[a.] School of Materials Science and Engineering, Zhengzhou University, Zhengzhou 450001, China

[b.] Key Laboratory of Green Printing, Institute of Chemistry Chinese Academy of Sciences (ICCAS), Beijing 100190, P. R. China. E-mail: sumeng1988@iccas.ac.cn; ylsong@iccas.ac.cn

[c.] School of Materials Science and Engineering, Dalian University of Technology, Dalian 116024, P. R. China

[d.] Institute of Polymers and Energy Chemistry, Nanchang University, Nanchang 330031, P. R. China. E-mail: happyhu@ncu.edu.cn

[e.] College of Chemistry, Zhengzhou University, Zhengzhou, 450001, P. R. China. E-mail: yqzhang@zzu.edu.cn.

[‡] These authors contributed equally to this work.

Experimental Section

Materials

Glass/ITO and PEN/ITO were purchased from South China Xiang Science and Technology Company, Ltd.. The SnO_2 colloid precursor was purchased from Alfa Aesar (tin (IV) oxide, 15 wt% in H_2O colloidal dispersion). Lead (II) iodide (PbI_2) was purchased from GreatCell Solar. Formamidine iodide (FAI), Methylammonium bromide (MABr), Methylammonium chloride (MACl), Cesium Iodide (CsI), 2,2,7',7'-tetrakis (N,N-di-4-methoxyphenylamine)-9,9'-spirobifluorene (Spiro-OMeTAD), 4-tert-butylpyridine (tBP) and Bis(trifluoromethylsulfonyl) amine lithium salt (Li-TFSI) were purchased from Xi'an Polymer Light Technology Corp. Chlorobenzene (CB) and isopropanol (IPA) were obtained from J&K. Dimethylformamide (DMF), dimethyl sulfoxide (DMSO), acetonitrile, ethylene glycol dimethacrylate (EGDMA) and poly(ethylene glycol) dimethacrylate (PEGDMA, Mn=550) were purchased from Sigma-Aldrich. All chemicals were used without any further purification process.

Perovskite Solar Cell Fabrication

Glass/ITO and PET/ITO were cleaned by sonication in detergents/H_2O, distilled water, and isopropanol for 20 min sequentially, then dried by N_2 blowing and treated by UV-ozone for 30 min. Then, a uniform and dense SnO_2 layer was deposited onto an ITO substrate by spin-coating SnO_2 nanoparticle solution (2.67% in H_2O) at 4000 rpm for 30 s, and annealed in ambient air at 120 ℃ for 40 min. After cleaning the SnO_2 substrate with ultraviolet ozone for 10 min, 645.41 mg PbI2, 18.19 mg CsI, 28.69 mg MACl, 170.94 mg FAI, 11.91 mg MABr in 0.8 mL anhydrous DMF and 0.2 mL anhydrous DMSO mixture solvent DMF/DMSO mixed solvent (8:2) was spin-coated onto SnO_2 by two consecutive spin-coating steps (1000 rpm 10 s and 5000 rpm 30 s), and 120 μL of CB with different PEGDMA concentration was dropped onto the spinning samples at the 25th second of the second step to form a brown film. Then, the film was annealed at 150 ℃ for 10 min. The PEGDMA would self-polymerize during the annealing and crystallization of the perovskite film due to its cross-linking polymerization property at high temperature. Next, Spiro-OMeTAD was dissolved in chlorobenzene to prepare Spiro-OMeTAD solution with a concentration of 72.3 mg/mL, then 17.5 μL of lithium bis(trifluoromethanesulfonyl)imide in acetonitrile (520 mg/mL) and 30 μL of 4-tert-butylpyridine were added into the Spiro-OMeTAD solution. The Spiro-OMeTAD solution was

spin-coated onto the perovskite film at 4000 rpm for 30 s. Finally, an 80 nm of Au film was deposited as a counter electrode. The area of shadow mask is 0.04 cm^2.

Films Characterization

The morphologies of the perovskite films and the devices were measured by field emission scanning electron microscopy (FE-SEM, Hitachi, S-4800 at 5 kV, 10 mA) and the microscopic atomic force microscopy (AFM) (nanoscope multimode Bruker). The thermogravimetric analyzer (TGA) was performed on the TGA 8000 at temperature from 25 to 400 ℃. The heating rate is 10 ℃/min. Fourier transform infrared (FTIR) spectra were recorded in transmittance mode using IR spectrometer instrument (Bruker, Tensor-27). The NMR spectra were measured on a Bruker Avance III (FT, DCH Cryoprobe, 400 MHz) spectrometer under ambient temperature. The XRD characterization of the samples were collected by using a X'Pert powder X-ray diffractometer (Bruker D8) with monochromatic Cu Kα radiation (λ = 1.5418 Å) operated at 40 kV and 40 mA. The GIXRD measurements were characterized using a Rigaku SmartLab 9Kw. GIWAXS measurements were performed using a Xeuss 2.0 spectrometer (Xenocs company) with MetalJet-D2 (Excillum) as the X-ray source and Pilatus 3R 1M (Dectris) as the detector. The absorption spectra were provided by the UV/vis spectroscopy (Shimadzu, UV-3600). Under the excitation at 485 nm, the steady-state photoluminescence (PL) and time-resolved photoluminescence (TRPL) tests were performed using steady state and lifetime spectrometer (FLS980, Edinburgh Instruments Ltd.). Laser scanning confocal microscopy (LSCM) images were obtained using NIS-Elements AR software on a confocal microscopy (Nikon Eclipse Ti). XPS and UPS measurements were recorded on a surface analysis system of AXIS Ultra DLD (Kratos Analytical) with ultrahigh vacuum.

Devices Characterization

The *J-V* curves of the PSCs were obtained by using a Keithley 2400 Source Meter under simulated one-sun AM 1.5G illumination (100 mW cm^{-2}) with a solar simulator (Enli Tech), the reference silicon solar cell was corrected from NREL. All the measurements were performed under nitrogen at room temperature. The devices were measured both in reverse scan (1.2 V→0 V, step 0.02 V) and forward scan (0 V→1.2 V, step 0.02 V), and the active area was defined by a shadow mask (0.04 cm^2). The light intensity was calibrated by a standard silicon cell with KG-5 filter. Steady-state power conversion efficiency was calculated by measuring stabilized photocurrent density under constant bias voltage (Vmax point). The

incident photo-to-electron conversion efficiency spectra (IPCE) were conducted by a monochromatic illumination optical system (Enli Tech, QE-R) with wavelength from 300 to 900 nm, calibrated by a Si reference solar cell. The repeated bending cycle tests are performed by a custom-made stretching machine, which was actuated by a stepper motor (Beijing Zhongke J&M). The EIS characteristics were determined on an electrochemical analyzer (ZAHENR, Germany). All the results of bending tests were averaged from over 50 samples.

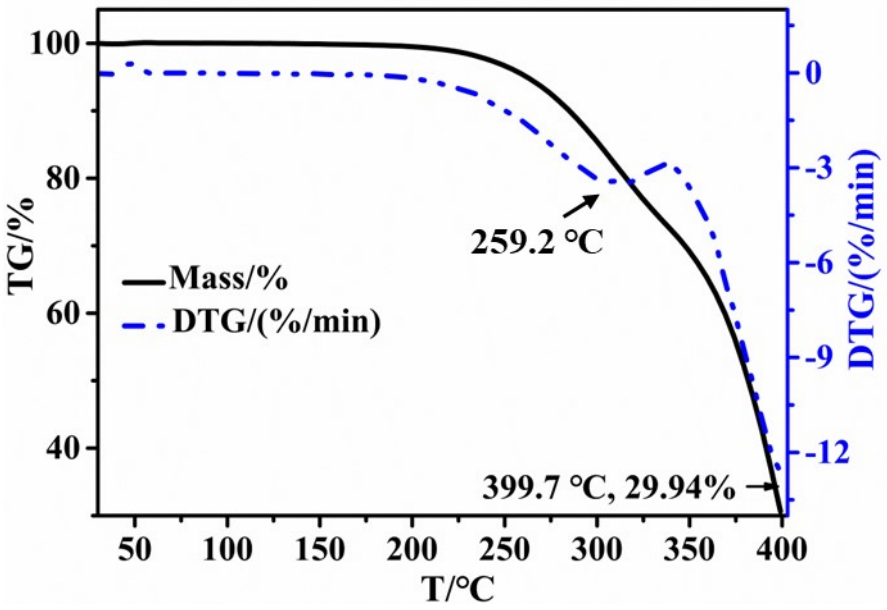

Fig. S1. Thermogravimetric analysis (TGA) of PEGDMA. The PEGDMA exhibits excellent thermostability with the decomposition temperature up to 250 ℃, much higher than the processing temperatures (~150 ℃) for the perovskite films in our experiments, making ensure that the SMPU remains in the perovskite films after the processing.

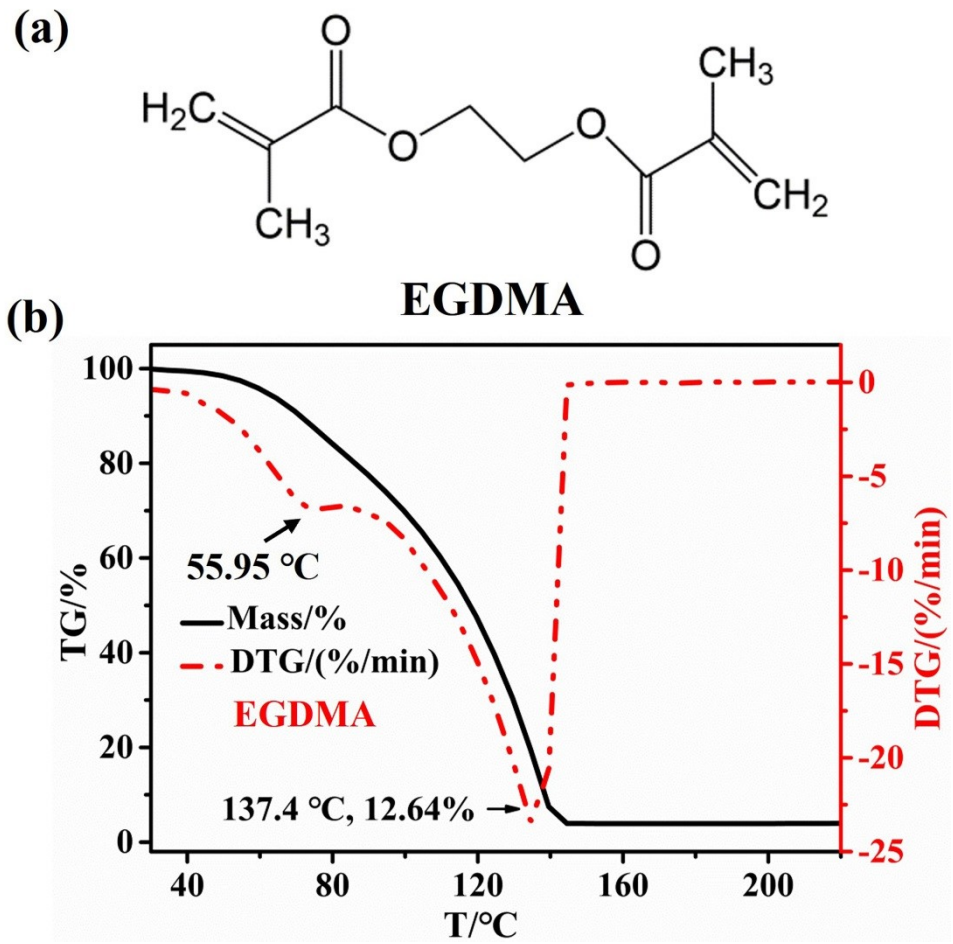

Fig. S2. (a) Molecular structure of EGDMA. (b) TGA of EGDMA. The thermal decomposition temperature of EGDMA is about 130 ℃, which is lower than the annealing temperature of 150 ℃ for perovskite, so it cannot effectively participate in the whole process of perovskite film crystal growth.

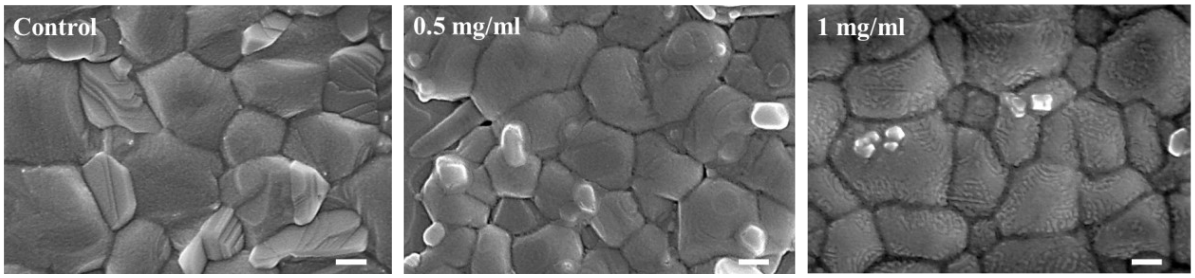

Fig. S3. Top-view SEM images of perovskite films with different concentrations of EGDMA (Scale bar: 200 nm). The grain size of the perovskite film with the addition of EGDMA monomer did not change significantly, but the grain boundaries effectively filled the polymer, indicating that the addition of monomer can reduce the grain boundaries defects.

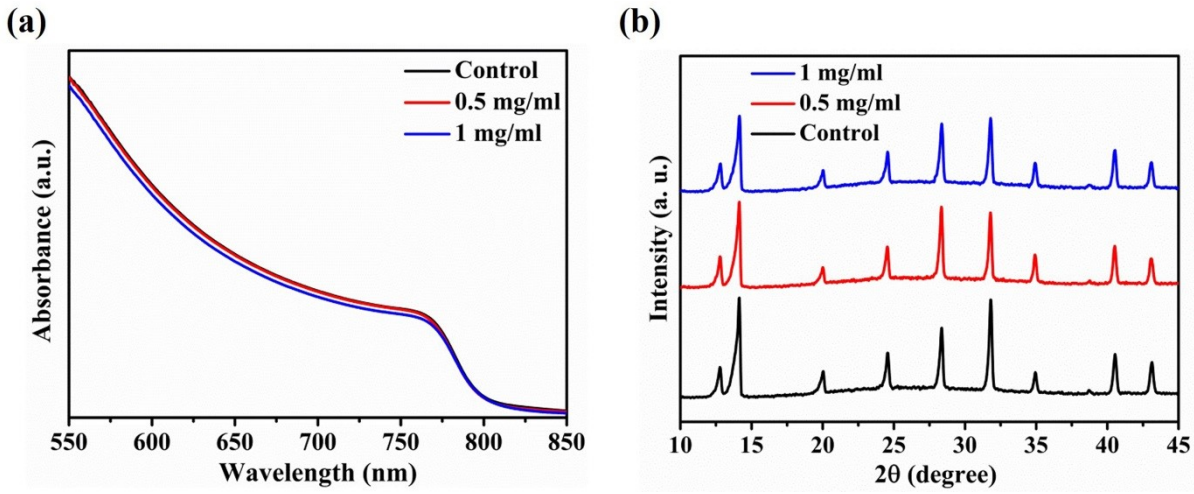

Fig. S4. (a) UV/Vis absorption spectra and (b) X-ray diffraction (XRD) patterns of the control and EGDMA-added perovskite films. Compared with the reference films, there is no obvious UV/Vis absorption edge and crystallization peak change of the X-ray diffraction (XRD) pattern in the EGDMA-added films.

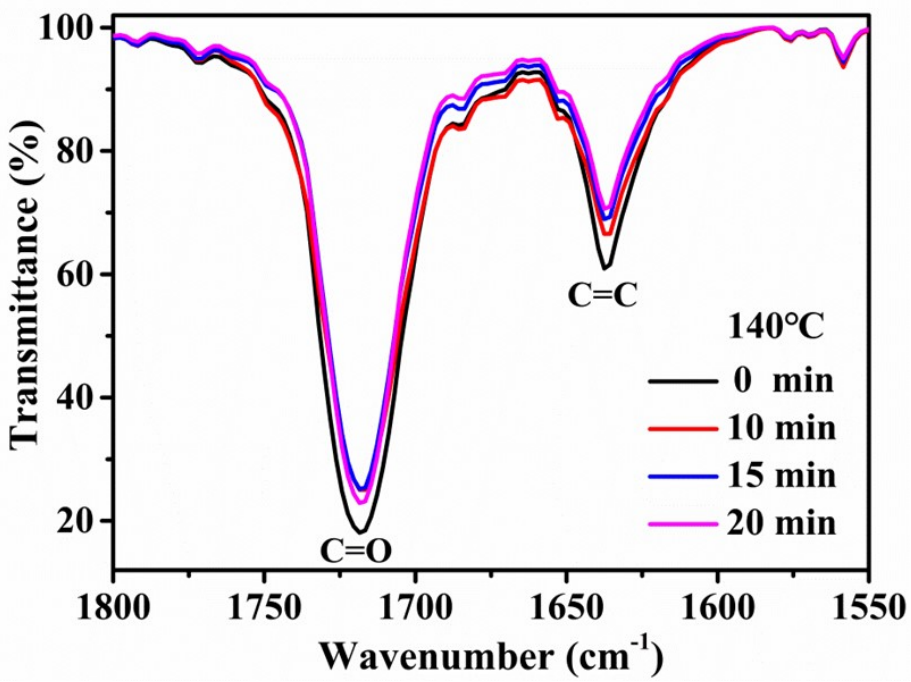

Fig. S5. FT-IR spectra of PEGDMA heated at 140 ℃ for different time. The results show that the C=O peak (1720 cm^{-1}) is relatively stable, while the C=C peak (1639 cm^{-1}) gradually decreases with the increase of heating time.[1]

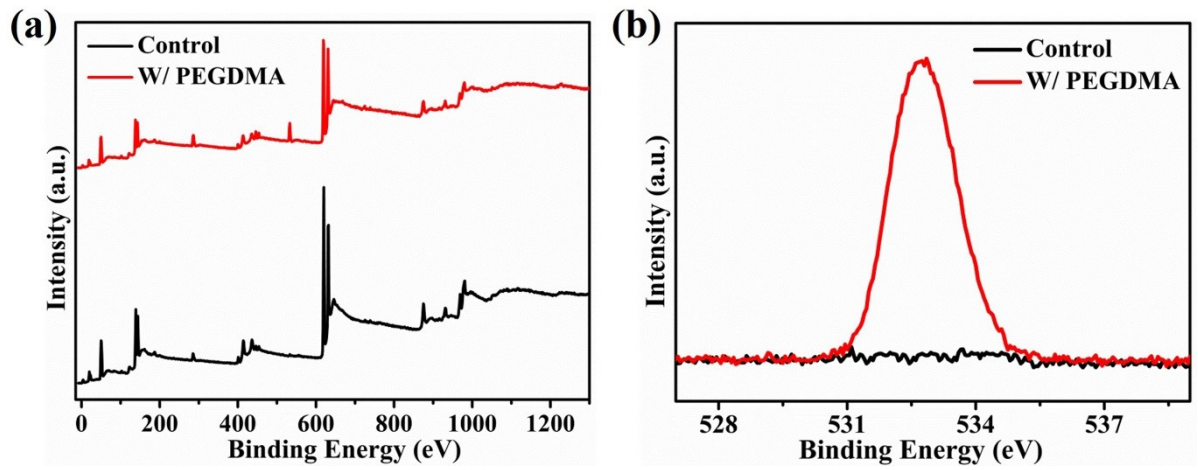

Fig. S6. XPS spectra of (a) entire elements and (b) O 1s for the control and PEGDMA-added perovskite film. The O 1s peak also verifies the successful introduction of O atoms into the perovskite films.

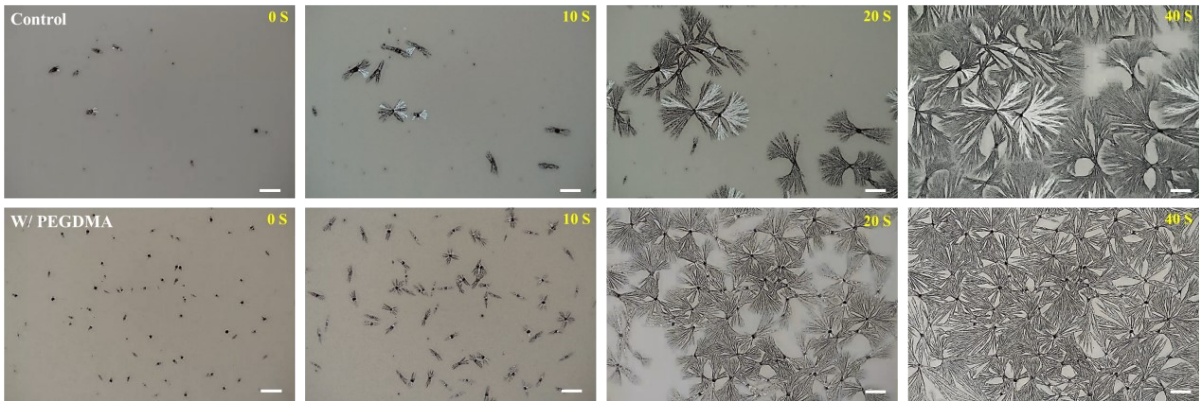

Fig. S7. The optical images of the crystallization nucleation process of perovskite films (Scale bar: 10 μm). At 0 s, several agglomerated nuclei appear in the control perovskite film, which grow rapidly and disorderly after 40 s. Interestingly, the PEGDMA-added films formed more uniform nuclei. Over time, multiregional crystals orderly grow in the whole film.

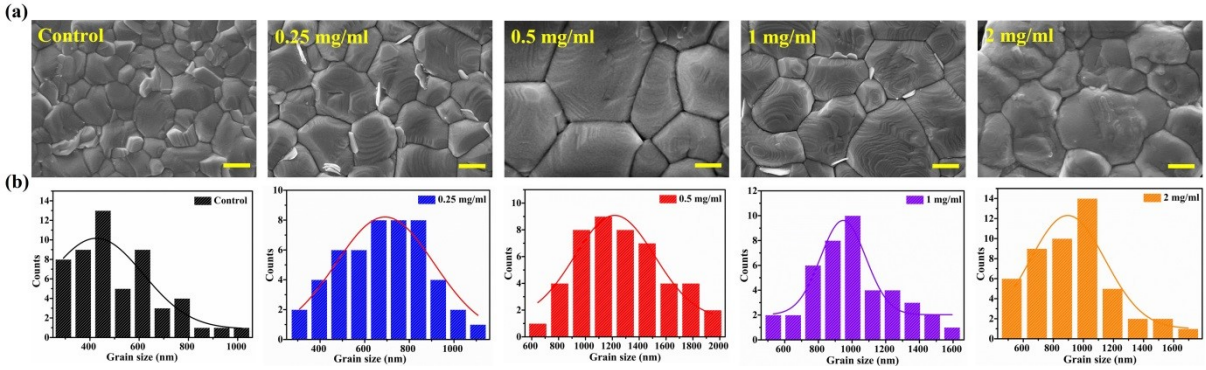

Fig. S8. Top-view SEM images and corresponding histogram of final grain size for the perovskite film with different PEGDMA contents (Scale bar: 500 nm). The grain size of the control perovskite film is approximately 510 nm. Compared with the control perovskite film, the grain size of the films with PEGDMA increased significantly (0.25, 0.5, 1, 2 mg/ml), and the maximum grain size is about 1200 nm when adding 0.5 mg/ml PEGDMA. The results indicate that PEGDMA is beneficial for regulating the growth of perovskite film.

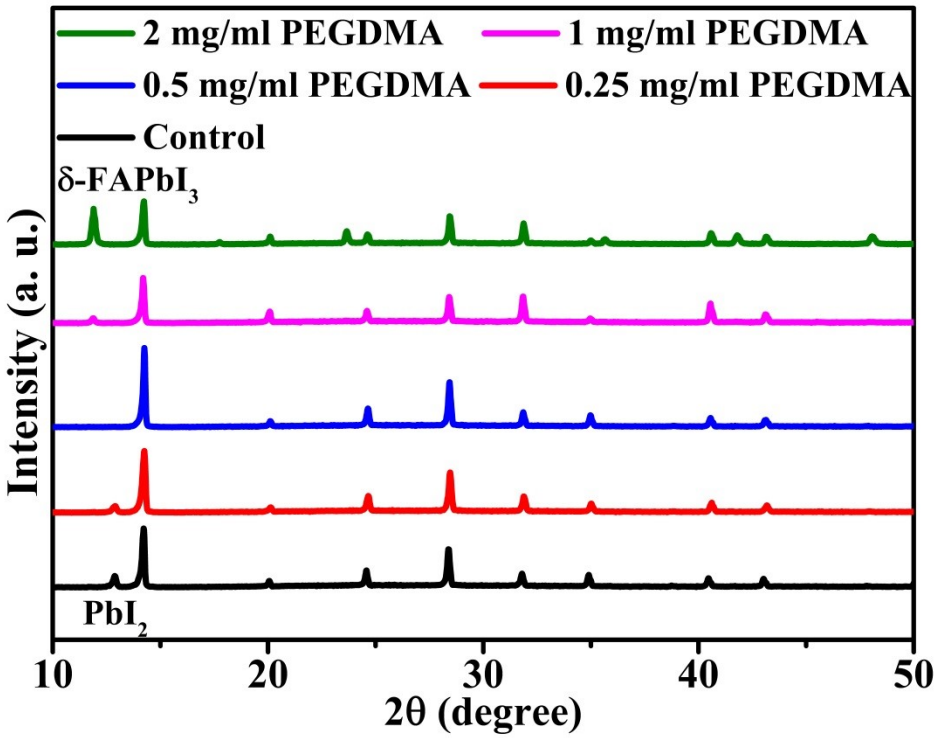

Fig. S9. XRD patterns of perovskite film with different PEGDMA contents. It is found that the remarkable PbI_2 peak located at 12.7° is obviously weakened or disappeared, indicating that the formation of PbI_2 has been inhibited to an appropriate amount, which is more conducive to the passivation grain boundary defects. In addition, the δ-$FAPbI_3$ appears with the increase of PEGDMA concentration, which limits the stability of the film. Therefore, 0.5 mg/ml is the most suitable addition amount.

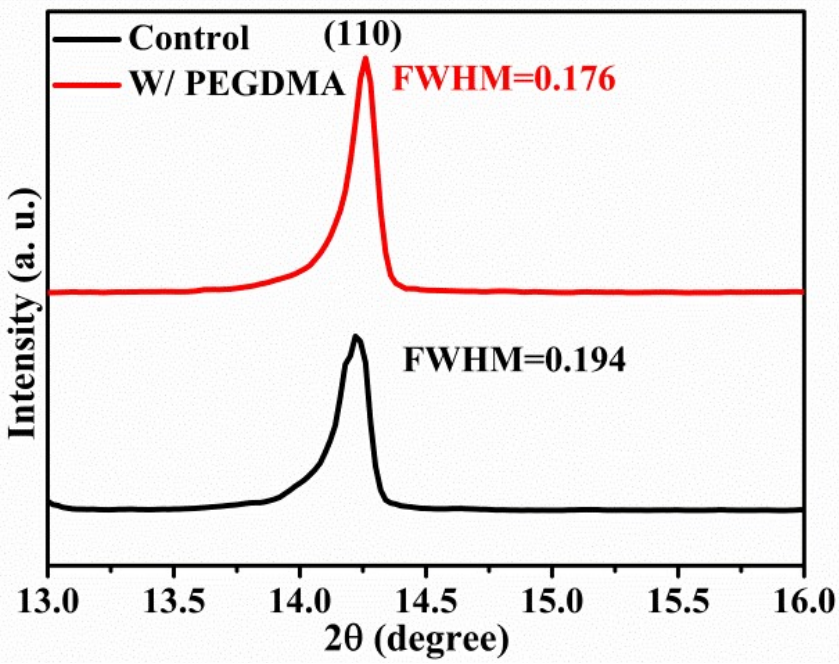

Fig. S10. (a) Magnification (110) X-ray diffraction (XRD) patterns of the control and PEGDMA-added perovskite films. The XRD peaks are fitted by the Voigt function. The FWHM value of the PEGDMA-added perovskite film at (110) crystal planes is 0.176, while the reference value is 0.194. The above results demonstrate that the crystallinity of the perovskite films can be significantly improved by incorporating PEGDMA.

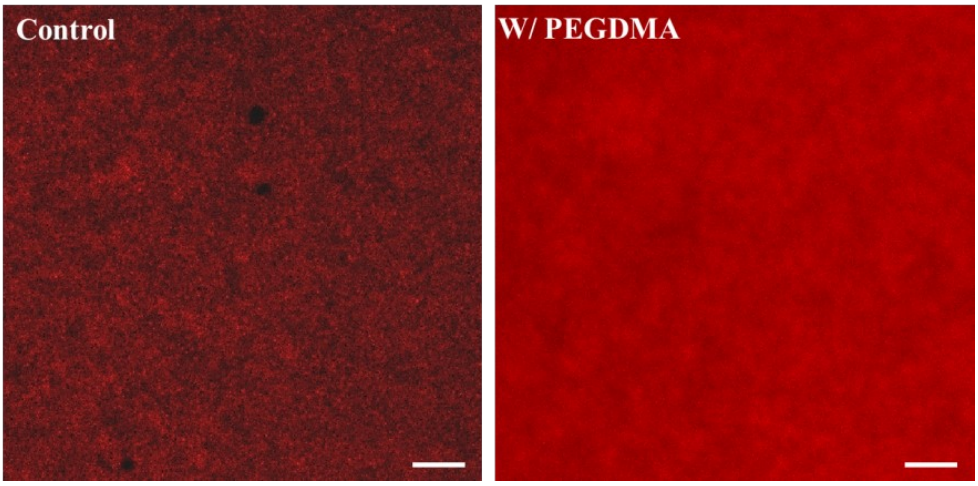

Fig. S11. Laser scanning confocal PL mapping images of the control and PEGDMA-added perovskite films (Scale bar: 10 μm). It indicate that PEGDMA-added perovskite films have the uniform red emission range from 700 to 800 nm, while many black holes are randomly distributed on the control film. These phenomena are consistent with the PL results.

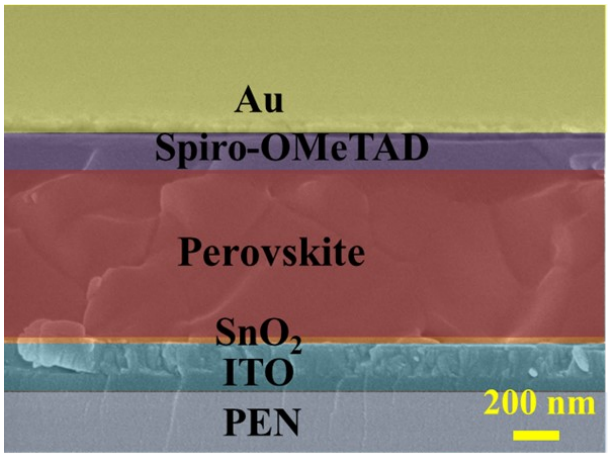

Fig. S12. Cross-sectional SEM image of the control device.

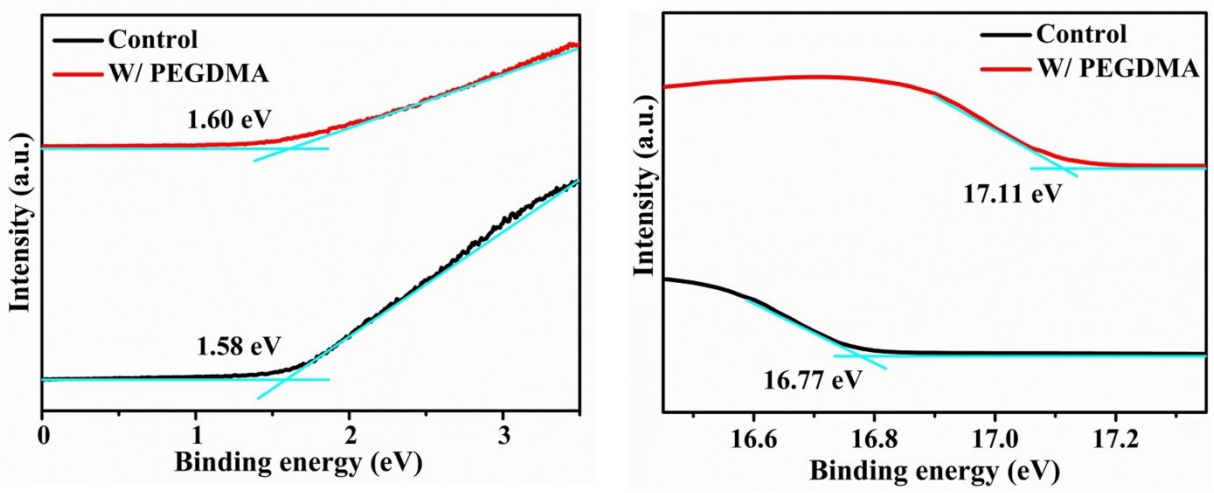

Fig. S13. UPS spectra of control and PEGDMA perovskite films for (a) low binding energy region, (b) high binding energy region.

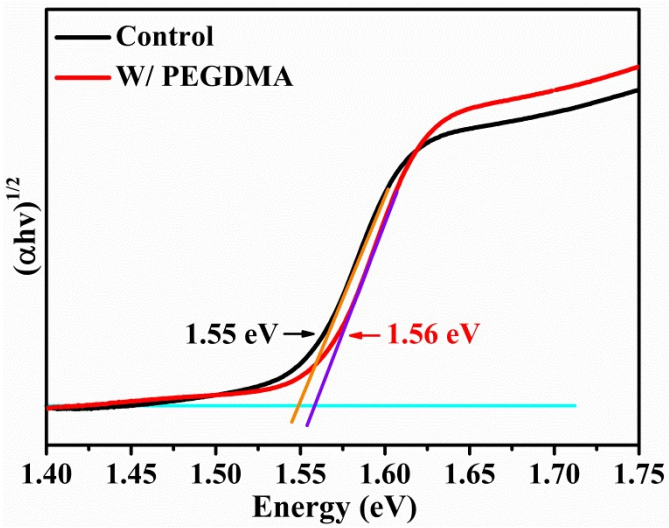

Fig. S14. The bandgap of the perovskite films calculated from UV-vis spectra.

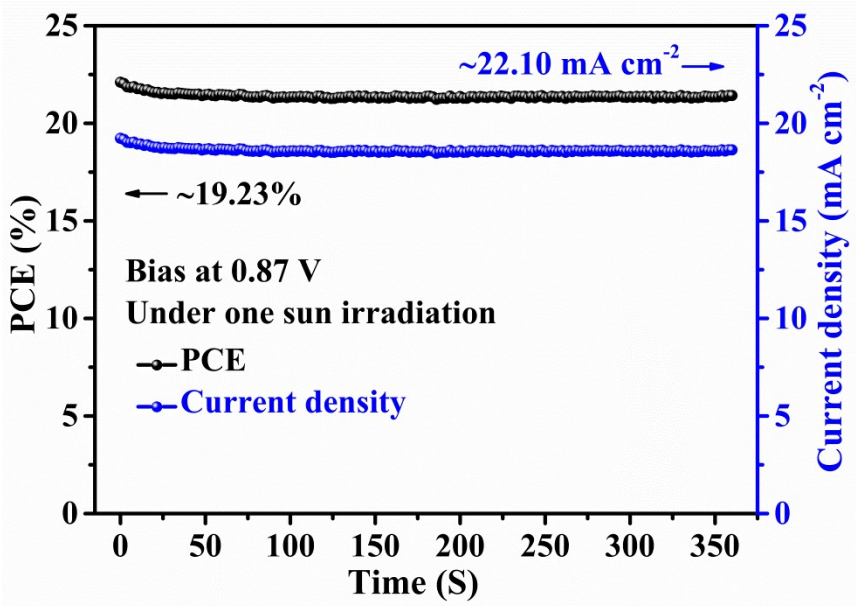

Fig. S15. The stabilized output power and photocurrent of the control flexible PSCs measured under a constant bias voltage (0.87 V) near the maximum power point.

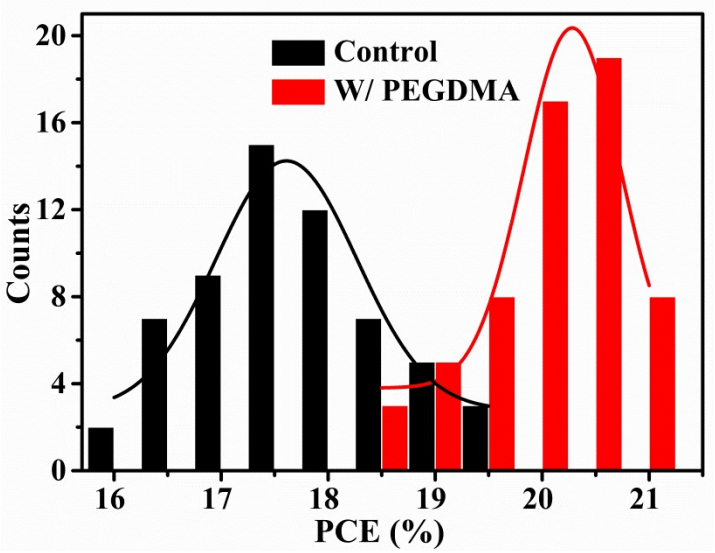

Fig. S16. Histograms of the PCE distribution among 60 flexible devices with and without PEGDMA.

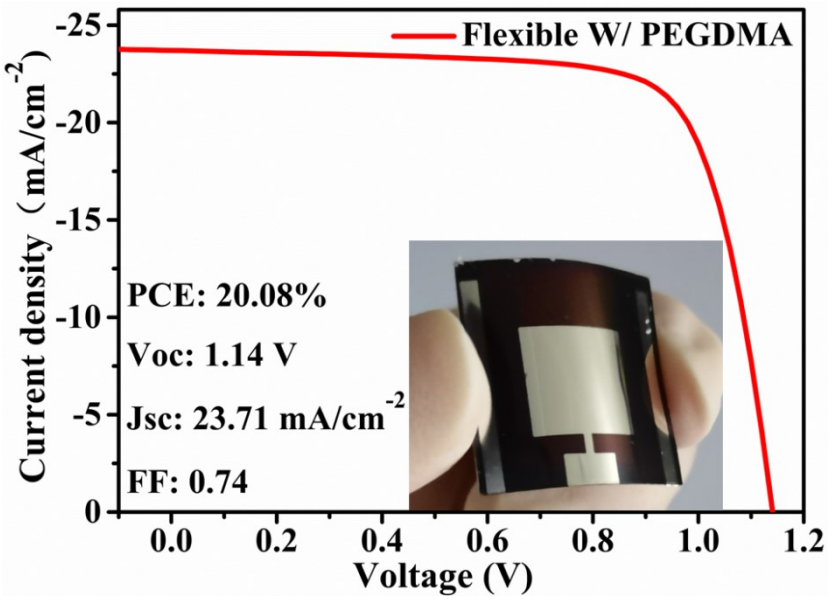

Fig. S17. The J-V curves of the large area flexible PSCs with PEGDMA. The inset photograph shows a large-area flexible PSC.

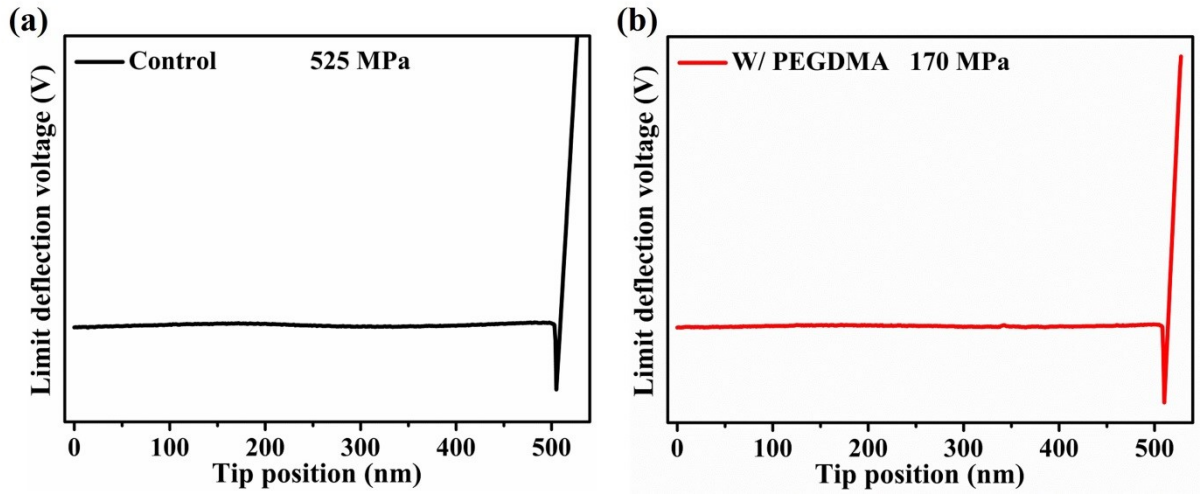

Fig. S18. Young's Modulus of the control and PEGDMA-added perovskite film measured by the peak-force model of AFM.

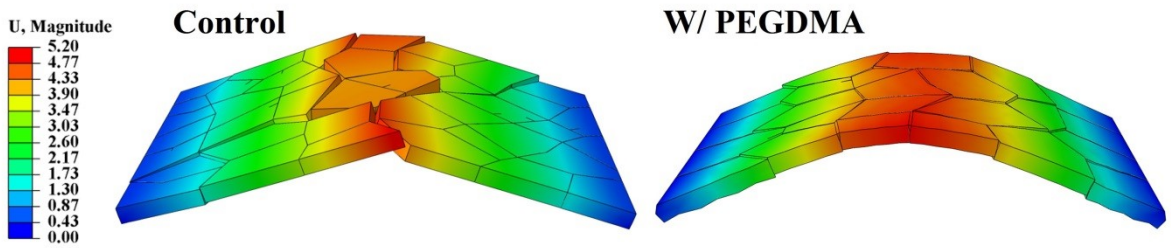

Fig. S19. The finite element analysis of the displacement distribution of the control and PEGDMA-added perovskite films under large bending deformation. Under the same bending defelection, the control perovskite film has obvious cracks. While, the PEGDMA-added perovskite film is still relatively intact.

A cohesive zone model is employed to simulate the fracture evolution and crack propagation in polycrystalline solids. The simulation samples are constructed though the part module of Abaqus/CAE. The cohesive elements are distributed at the grain boundaries of perovskite films. A constitutive model of cohesive elements with linear elasticity-linear softening is adopted to simulate the stress distribution of perovskite films under different bending deflections. Quadratic nominal stress criterion (Quads damage) is used to judge initial damage. The quads damage can be described as[2]:

$$\left\{\frac{\sigma_n}{\sigma_n^0}\right\}^2 + \left\{\frac{\tau_s}{\tau_s^0}\right\}^2 + \left\{\frac{\tau_t}{\tau_t^0}\right\}^2 = 1$$

σ^0_n, τ^0_s, τ^0_t represent normal stress, stress in the first shear direction, and stress in the second shear direction of cohesive elements, respectively. In this manuscript, the cohesive zone parameters are measured by ASDM D897[3] and ASTM D1002[4]. The corresponding mechanical properties of cohesive elements used for finite-element simulation via abaqus software are shown in **Table S7**.

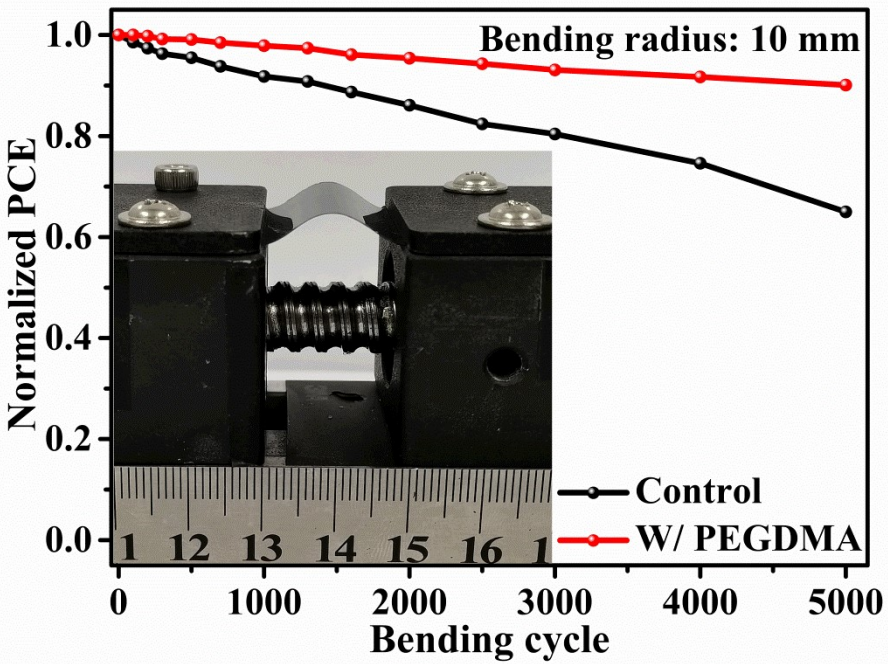

Fig. S20. Normalized average PCE of PSCs as a function of bending cycles with bending radius of 10 mm.

Table S1. The characteristic peak intensities and ratios in the XRD patterns.

Content	(110)	(310)	(110)/(310)
Control	1849	444	4.16
W/ PEGDMA	2477	482	5.13

Table S2. The half-width of peak strength of the perovskite films with and without PEGDMA.

Content	Main peak position (°)	FWHM (main peak)
Control	14.22	0.194
W/ PEGDMA	14.26	0.176

Table S3. τ_1 and τ_2 from PL decay spectra with different samples.

Samples	τ_1 (ns)	A_1 (%)	τ_2 (ns)	A_2 (%)	τ(ns)
Control	153.58	6.64	588.96	93.36	560.05
W/ PEGDMA	105.93	1.18	1155.43	98.82	1143.05

The PL decay fitting curve is based on a bi-exponential rate law:

$f(t)= A_1\exp(-\tau/\tau_1)+A_2\exp(-\tau/\tau_2)+y_0$

Where A_1 and A_2 represent the decay amplitude, τ_1 represents trap-assisted recombination, andτ_2 demonstrates free carrier recombination, and y_0 is a constant.

Table S4. Calculated parameters of the control and PEGDMA incorporated device from UPS.

Devices	E_{cutoff} (eV)	E_F (eV)	E_{onset} (eV)	E_{VBM} (eV)	E_g (eV)	E_{CBM} (eV)
Control	16.77	4.45	1.58	6.03	1.55	4.48
W/ PEGDMA	17.11	4.11	1.60	5.71	1.56	4.15

where the Fermi energy: E_F =21.22 eV (*He I*)−E_{cutoff}

Valence band maximum energy: $E_{VBM}=E_{onset}+E_F$

Conduction band minimum energy: $E_{CBM}=E_{VBM}+E_g$

Table S5. Performances of several representative flexible PSCs for comparison with this work.

Configuration	Notes	Effective area (cm^2)	PCE (%)	Ref.
PET/ITO/SnO_2/C60-SAM/PVK/Spiro-OMeTAD/Au	$Pb(SCN)_2$ additive	0.08	17.96	5
PET/ITO/PVK:C-PCBOD/Spiro-OMeTAD/MoO_3/Ag	Grains embraced $MAPbI_3$:C-PCBOD	0.07	18.1	6
MgF_2/PET/ITO/Nb_2O_5/PVK-DS/ Spiro-OMeTAD/Au	Dimethyl sulfide additive	0.052	18.40	7
PDMS/hc-PEDOT:PSS/PEDOT:PSS Al4083/PVK/PCBM/ polyethyleneimine(PEI)/hc-PEDOT:PSS /PDMS	dynamic oxime-carbamate bonds self-healing	0.16	19.15	8
PDMS/hc-PEDOT:PSS/PEDOT:PSS Al4083/PVK/PCBM/ hc-PEDOT:PSS/PDMS	Hydrogen bonding self-healing	0.09	19.5	9
PDMS/PEDOT:PSS/PEDOT:PSS/ PVK/PEI/PEDOT:PSS/PDMS	Elastic ''brick-and-mortar'' structure	1.0	19.59	10
MgF_2/Willow Glass/ITO /PTAA/$MAPbI_3$/C60/BCP/Cu	NH_4Cl addition	0.08	19.72	11
FG/ITO/PTAA/PFN-Br/PVK/ C60/BCP/Cu	elastic grain boundary encapsulation	-	20	12
PEN/ITO/FI-SnO_2/PVK Spiro-OMeTAD/Au	FI-SnO_2/perovskite interface	0.16	20.1	13
PET/hc-PEDOT:PSS/ PVK:s-GO/PCBM/Ag	s-GO-modified perovskite film	1.01	20.56	14
PET/ITO/SnO_2/ LD/3D MHP/Spiro-OMeTAD/Au	LD MHP capping layer	0.096	21.0	15
PEN/ITO/HfO_x/SnO_2/PVK/ Spiro-OMeTAD/Au	artemisinin-doped perovskite layer	-	21.1	16
PEN/ITO/SnO_2/PVK/ Spiro-OMeTAD/Au	**In-situ cross-linking polymerization of PEGDMA**	**0.04**	**21.41**	**This work**

Table S6. Photovoltaic parameters of the flexible PSCs (0.04 cm^2) with PEGDMA.

Sample No.	Jsc (mA cm^{-2})	Voc (V)	FF	PCE (%)
1	24.27110157	1.150150324	76.69794	21.41055
2	24.24566279	1.144459307	75.45304	20.93684
3	24.09041655	1.122199986	74.91449	20.25258
4	24.37060262	1.116017872	74.40629	20.23704
5	23.54741184	1.129359151	77.22492	20.5368
6	23.70774018	1.136581804	76.69359	20.66569
7	23.81994069	1.165699222	75.56333	20.98158
8	24.24423699	1.165817183	72.96236	20.62233
9	24.12443981	1.157486514	72.68335	20.29589
10	23.96893688	1.157002951	73.61094	20.41388
11	24.36109498	1.151092864	74.1847	20.80279
12	23.8087168	1.14744902	71.30806	19.48085
13	23.54741184	1.129359151	77.22492	20.5368
14	23.47089641	1.130253061	75.67214	20.07435
15	23.71312759	1.130762905	75.5389	20.25494
16	24.11959314	1.135341607	75.67156	20.72188
17	24.42648198	1.158246013	74.3634	21.0388
18	23.611465	1.126699939	72.41716	19.26516
19	23.34761142	1.133125063	72.8478	19.27244
20	23.78781384	1.090976297	76.93249	19.96547
21	24.13894777	1.10034894	76.16403	20.23013
22	24.10788351	1.09306917	75.61367	19.9254
23	24.11619294	1.121631306	76.94465	20.81312
24	23.783613	1.142603439	73.98412	20.10536
25	24.34903086	1.132385139	77.16692	21.27684
26	23.83898303	1.138187875	73.02265	19.81341
27	24.29265558	1.141196885	74.35346	20.61279
28	23.53225631	1.125616995	74.56367	19.75065
29	23.41736952	1.123690907	76.0218	20.00429
30	24.28705746	1.134641408	76.79212	21.16168

Table S7. Cohesive zone model parameters for the finite-element simulation.

Parameter	Normal stress (N/m^2)	1st direction Shear strength (N/m^2)	2nd direction shear strength (N/m^2)	Normal fracture energy (N/m)	1st Shear fracture energy (N/m)	2nd Shear fracture energy (N/m)
Value	100000	80000	80000	100	120	120

References

1. B. Niu, H. Wu, J. Yin, B. Wang, G. Wu, X. Kong, B. Yan, J. Yao, C.-Z. Li, H. Chen, *ACS Energy Lett.,* 2021, **6**, 3443-3449.

2. M. A. Bellali, B. Serier, M. Mokhtari, R. D. S. G. Campilho, F. Lebon, H. Fekirini, *Compos. Struct.,* 2021, **266**, 113805.

3. G. L. Anderson, *J. Adhes.,* 2006, **41**, 129-137.

4. H. Y. Yeh, D. Tandjung, J. Reinf. *Plast. Compos.,* 2016, **24**, 839-853.

5. C. Wang, D. Zhao, Y. Yu, N. Shrestha, C. R. Grice, W. Liao, A. J. Cimaroli, J. Chen, R. J. Ellingson, X. Zhao, Y. Yan, *Nano Energy,* 2017, **35**, 223-232.

6. M. Li, Y. G. Yang, Z. K. Wang, T. Kang, Q. Wang, S. H. Turren-Cruz, X. Y. Gao, C. S. Hsu, L. S. Liao, A. Abate, *Adv. Mater.,* 2019, **31**, e1901519.

7. J. Feng, X. Zhu, Z. Yang, X. Zhang, J. Niu, Z. Wang, S. Zuo, S. Priya, S. F. Liu, D. Yang, *Adv. Mater*., 2018, **30**, e1801418.

8. X. Meng, Z. Xing, X. Hu, Z. Huang, T. Hu, L. Tan, F. Li, Y. Chen, *Angew. Chem. Int. Ed.,* 2020, **59**, 16602-16608.

9. K. Zhang, Y. Deng, X. Shi, X. Li, D. Qi, B. Jiang, Y. Huang, *Angew. Chem. Int. Ed.,* 2022, **61**, e202112673.

10. X. Hu, Z. Huang, F. Li, M. Su, Z. Huang, Z. Zhao, Z. Cai, X. Yang, X. Meng, P. Li, Y. Wang, M. Li, Y. Chen, Y. Song, *Energy Environ. Sci.,* 2019, **12**, 979-987.

11. X. Dai, Y. Deng, C. H. Van Brackle, S. Chen, P. N. Rudd, X. Xiao, Y. Lin, B. Chen, J. Huang, *Adv. Energy Mater.,* 2019, **10**, 1903108.

12. C. Ge, Z. Yang, X. Liu, Y. Song, A. Wang, Q. Dong, *CCS Chem.,* 2021, **3**, 2035-2044.

13. Q. Dong, C. Zhu, M. Chen, C. Jiang, J. Guo, Y. Feng, Z. Dai, S. K. Yadavalli, M. Hu, X. Cao, Y. Li, Y. Huang, Z. Liu, Y. Shi, L. Wang, N. P. Padture, Y. Zhou, *Nat. Commun.,* 2021, **12**, 973.

14. X. Hu, X. Meng, X. Yang, Z. Huang, Z. Xing, P. Li, L. Tan, M. Su, F. Li, Y. Chen, Y. Song, *Sci. Bull.*, 2021, **66**, 527-535.

15. Q. Dong, M. Chen, Y. Liu, F. T. Eickemeyer, W. Zhao, Z. Dai, Y. Yin, C. Jiang, J. Feng, S. Jin, S. Liu, S. M. Zakeeruddin, M. Grätzel, N. P. Padture, Y. Shi, *Joule*, 2021, **5**, 1587-1601.

16. L. Yang, Q. Xiong, Y. Li, P. Gao, B. Xu, H. Lin, X. Li, T. Miyasaka, *J. Mater. Chem. A,* 2021, **9**, 1574-1582.